Observation of Dirac nodal line states in topological semimetal candidate PrSbTe

Dengpeng Yuan,[1,*] Dajian Huang,[1,*] Xin Ma,[2] Xu Chen,[3] Huifen Ren,[3] Yun Zhang,[1] Wei Feng,[1] Xiegang Zhu,[1] Bo Wang,[1] Xuwen He,[1] Jian Wu,[1] Shiyong Tan,[1] Qunqing Hao,[1] Qiang Zhang,[1] Yi Liu,[1] Qin Liu,[1] Zhengtai Liu,[4] Chao Cao,[2,†] Qiuyun Chen,[1,‡] and Xinchun Lai[1,§]

[1]*Science and Technology on Surface Physics and Chemistry Laboratory, Mianyang 621907, China*
[2]*Center for Correlated Matter and School of Physics, Zhejiang University, Hangzhou 310058, China*
[3]*Beijing National Laboratory for Condensed Matter Physics, Institute of Physics, Chinese Academy of Sciences, Beijing 100190, China*
[4]*Shanghai Synchrotron Radiation Facility, Shanghai Advanced Research Institute, Chinese Academy of Sciences, Shanghai 201210, China*

(Received 1 November 2023; accepted 20 December 2023; published 8 January 2024)

The interplay among topology, crystal symmetry, magnetic order, and strong electron correlation can give rise to a plethora of exotic physical phenomena. The ZrSiS family is known as typical topological Dirac semimetals, among them *Ln*SbTe (*Ln* denotes lanthanide) compounds exhibit intriguing characteristics due to the presence of *Ln* $4f$ electrons, resulting in quantum states and unique properties. In this paper, the topological electronic structure of PrSbTe is systematically studied by angle-resolved photoemission spectroscopy (ARPES), combined with magnetic, specific heat measurements, and band structure calculations. The detailed three-dimensional electronic structure of PrSbTe has been obtained, and a diamond-shaped Fermi surface and multiple Dirac nodal lines have been observed, which are in remarkable agreement with theoretical calculations. Moreover, the $4f$ electrons in PrSbTe are rather localized, which can be revealed by on-resonant ARPES data and further confirmed by the rather small Sommerfeld coefficient of $\gamma = 2.6231\ \mathrm{mJ/mol\,K^2}$. Our results provide more detailed information about the *Ln*SbTe family, which gives a deeper understanding of the interaction between *Ln* $4f$ electrons and the topological states.

DOI: 10.1103/PhysRevB.109.045113

I. INTRODUCTION

The topic of topological materials is one of the most important in the field of condensed matter physics. Although plenty of topological materials have been predicted theoretically, only a few of them have been verified experimentally. One way to find topological materials is to investigate the structural features by symmetry, which can fulfill the electronic features of the band structures, such as Dirac points formed by the band crossings. For example, it is well known that nonmagnetic square nets can give rise to Dirac node lines because nonsymmorphic symmetry satisfies energy band degeneracy [1,2]. The slip surface protects spin-orbit coupling (SOC) degeneracy, thus opening the hybridization band gap and preserving the Dirac nodal lines (DNLs). In the magnetic case, because of time-reversed symmetry breaking, the DNLs will break up into Weyl nodal lines [3,4]. From the structural characterization point of view, one way to look for symmetry-protected semimetals is to consider the crystal structures with square nets, which have also been observed in iron- and copper-based superconductors [5–8]. Among these, there has recently been rapidly growing attention to the ZrSiS family of topological nodal line semimetals protected by nonsymmorphic symmetry [9–11]. These compounds possess peculiar physical properties, such as large magnetoresistance [12,13] and high carrier mobility [14,15]. Therefore, prediction and experimental discovery of materials with topologically nontrivial electronic band structure are becoming a focus.

Recently, one isostructural subgroup of the ZrSiS materials, the *Ln*SbTe (*Ln* = La, Ce, Nd, Sm, Gd, Ho) compounds, has been gaining considerable interest, which offers great opportunities for exploring exotic phenomena arising from the interplay among topology, charge density wave (CDW), and the Kondo effect. This family of materials is confirmed to be topological semimetals by ARPES measurements [16–22] and shown to host nonsymmorphic topological fermions coming from the square-net plane of the Sb element and nodal line fermions. Due to the presence of $4f$ electrons, *Ln*SbTe compounds usually possess antiferromagnetically (AFM) ordered ground states [23–27]. For instance, CeSbTe is AFM below $T_N = 2.7$ K at zero field but undergoes a metamagnetic transition under a small field of ~ 0.25 T [16]. Furthermore, CDW states are commonly found in the nonstoichiometric *Ln*SbTe compounds [28–30]. The CDW vectors of nonmagnetic $LaSb_xTe_{2-x}$ can be continuously modulated along with the components of Sb [31]. Similarly, AFM $GdSb_xTe_{2-x-\delta}$ can be modulated into either proportional or disproportional lattice modulation, depending on the Sb content, with the CDW appearing in the ordered phases when $x < 1$ [32]. These investigations indicate that the *Ln*SbTe system is an ideal platform to search for exotic topological electronic states. However, the ground states of these compounds and their mutual interactions remain unsolved.

In this paper, we successfully synthesize a compound PrSbTe, which crystallizes into a nonsymmorphic structure.

*These authors contributed equally to this work.
†ccao@zju.edu.cn
‡chenqiuyun@caep.cn
§laixinchun@caep.cn

The paramagnetic state of PrSbTe remains down to 0.4 K, as indicated by the specific and magnetic measurements. The detailed three-dimensional electronic structure of this compound has been systematically obtained, and multiple symmetry-protected DNLs are observed in the bulk electronic band structure, even in the presence of the SOC. Resonant angle-resolved photoemission spectroscopy (ARPES) measurements reveal that the Pr $4f$ electrons are rather localized in this compound, which is consistent with its small Sommerfeld coefficient obtained by fitting specific heat data. Our findings enrich the ZrSiS family and extend the topological nodal line semimetals.

II. EXPERIMENTAL AND COMPUTATIONAL DETAILS

High-quality PrSbTe single crystals were synthesized by a chemical vapor transport method with iodine as the transport agent. Stoichiometric amounts of high-purity Pr (Alfa Aesar 99.9%), Sb (Alfa Aesar 99.999%), and Te (Sigma-Aldrich 99.9999%), along with ~ 90 mg of iodine (Alfa Aesar 99.999%), were placed into a 14-mm-internal-diameter quartz tube. The quartz tube was then sealed under vacuum ($< 5 \times 10^{-3}$ mbar) and put into a gradient furnace. A temperature gradient from 1000 to 900° C was maintained along the 200-mm-long tube for 14 d. After cooling, the samples were mechanically extracted from the cold end of the tube and washed with ethanol to dissolve residual iodine.

Millimeter-sized PrSbTe single crystals with metal luster were obtained. Single-crystal and powder x-ray diffraction (XRD) at room temperature was used to characterize the crystal structure of our samples. A powder sample was obtained by grounding single crystals. The magnetic measurements were characterized with a Quantum Design vibrating sample magnetometer from 0.4 to 300 K and up to 7 Tesla. Specific heat was measured from 2 to 300 K by the relaxation method in a Quantum Design physical property measurement system. ARPES measurements were performed at the BL03U Beamline of the Shanghai Synchrotron Radiation Facility (SSRF) [33] with a Scienta DA30L Analyzer, and the measurement temperature was maintained at $T = 10$ K. The combined resolution of beamline and spectrometer at $h\nu = 95$ eV amounts to 30 meV in energy and 0.1° in angular resolution. A clean surface of the sample was obtained by *in situ* cleaving along the (0 0 1) plane in an ultrahigh vacuum, and the vacuum was kept $< 7 \times 10^{-11}$ mbar.

Electronic structure calculations in this paper were performed using density functional theory (DFT) and a plane-wave basis projected augmented-wave method, as implemented in VASP [34,35]. The Perdew, Burke, and Enzerhoff [36] generalized gradient approximation for exchange-correlation potential was used for the DFT calculation. The $4f$ electrons of Pr were treated as localized core electrons, and SOC was considered in all calculations. An energy cutoff of 320 eV and a $12 \times 12 \times 6$ Monkhorst k-mesh were employed to converge the calculation to 1 meV/atom.

III. RESULTS

PrSbTe crystallizes into a PbFCl-type crystal structure with a tetragonal space group $P4/nmm$, as illustrated in Fig. 1(a). It is isostructural to the well-known 111-type iron-based superconductor LiFeAs [37]. A Te-Pr-Sb-Pr-Te slab forms the quintuple layers along the c axis, and the Pr-Te bilayers are sandwiched between the square-net Sb layers. Because of the weak bonding between two adjacent quintuple layers via van der Waals interactions, the crystals usually cleave easily at the Te termination along the (0 0 1) plane [21]. The powder XRD pattern is displayed in Fig. 1(c), and refined lattice parameters are $a = b = 4.358(4)$ Å and $c = 9.391(3)$ Å, which are in accordance with the previously reported results [38]. The XRD patterns on a flat surface of a PrSbTe single crystal at ambient conditions are shown in Fig. 1(b). Only sharp (0 0 l) peaks can be observed, which indicates PrSbTe single crystal has a natural cleavage plane perpendicular to the c axis. The full width at half maximum of the (0 0 3) peak in the rocking scan is $< 0.1°$, revealing high crystalline quality. The inset in Fig. 1(b) is an image of a typical PrSbTe single crystal with a size of $1.2 \times 1 \times 0.5\,\text{mm}^3$.

The temperature-dependent magnetic susceptibility $\chi = M/H$ and inverse magnetic susceptibility $1/\chi$ with $H//c$ of PrSbTe under an applied magnetic field of 0.1 T are displayed in Fig. 1(d). When the temperature decreases to ~ 10 K, the abrupt enhancement in magnetic susceptibility $\chi(T)$ exhibits characteristics reminiscent of a ferromagnetic transition. Nevertheless, no significant hysteresis loop was observed in the isothermal magnetization curve until reaching the lowest temperature of 0.4 K, as shown in the inset of Fig. 1(e). On the other hand, $\chi(T)$ is found to follow the modified Curie-Weiss law $\chi_{\text{mol}} = \chi_0 + C/(T - \Theta)$ above 100 K, where χ_0 is the temperature-independent part of the susceptibility, C is the Curie temperature, and Θ is the Weiss temperature. The fitted Curie constant C yields an effective moment $\mu_{\text{eff}} = \sqrt{3k_B C/N_A} = 3.7\ \mu_B$, which is consistent with the theoretically predicted value of $\mu_{\text{eff}} = 3.6\ \mu_B$. The Weiss temperature $\Theta = -24.5$ K is negative, implying predominant AFM exchange interactions. For $T < 100$ K, the deviation of the inverse magnetic susceptibility curve from the Curie-Weiss fit has a similar trend to that observed in CeSbTe, which is attributed to the crystalline electric field effect [39].

The specific heat capacity (C_p) of PrSbTe at zero magnetic field is shown in Fig. 1(f). No anomalies were observed in the C_p curve, indicating the absence of phase transition down to 2 K for PrSbTe. Considering the contributions from electrons and phonons, the specific heat at low temperature can be expressed as $C_p = \gamma T + \beta T^3$, where γT represents the electronic contribution, and βT^3 denotes the phonon contribution. The C_p/T vs T^2 data < 8 K were fitted, as shown in the inset of Fig. 1(f). The derived Sommerfeld coefficient is $\gamma = 2.6231\,\text{mJ/mol K}^2$, indicating a small electronic contribution to the specific heat. Compared with GdSbTe ($\gamma = 7.6\,\text{mJ/mol K}^2$) [23], CeSbTe ($\gamma = 41\,\text{mJ/mol K}^2$) [39], NdSbTe ($\gamma = 115\,\text{mJ/mol K}^2$) [24], SmSbTe ($\gamma = 160\,\text{mJ/mol K}^2$) [20], and HoSbTe ($\gamma = 382.2\,\text{mJ/mol K}^2$) [25], the small value of the Sommerfeld coefficient γ for PrSbTe indicates the localized nature of its $4f$ electrons. Although the Sommerfeld coefficients γ of LnSbTe exhibit a strong dependence on the choice of Ln element, the obtained phonon coefficient $\beta = 0.5682\,\text{mJ/mol K}^4$ yields a comparable Debye temperature $\Theta_D = 217.3$ K with other

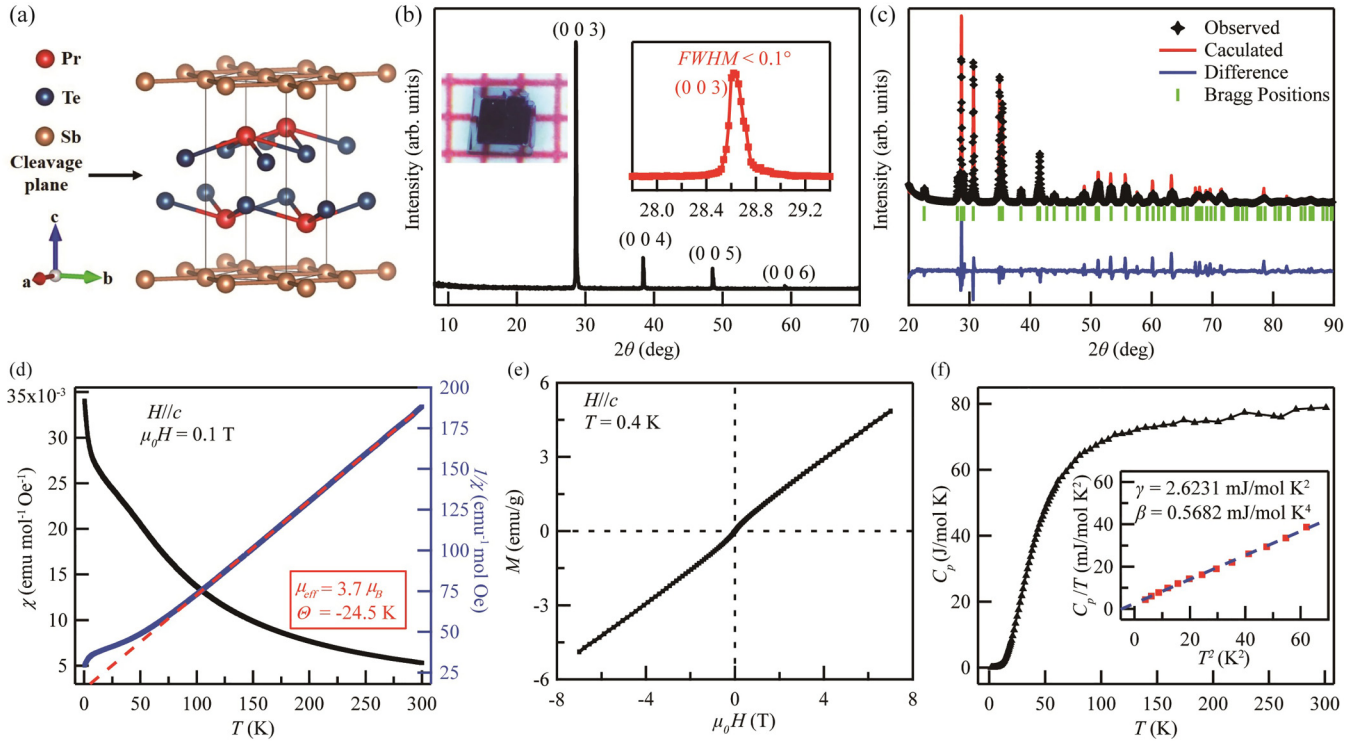

FIG. 1. (a) Crystal structure of PrSbTe as determined by single-crystal x-ray diffraction (XRD). The black arrow denotes the natural cleaving termination. (b) XRD pattern of PrSbTe single crystals. Only sharp (0 0 l) peaks can be observed. Inset: Image of PrSbTe single crystal (the back square is $1 \times 1\,\mathrm{mm}^2$; left); enlarged XRD pattern around the (0 0 3) reflection peak (right). (c) Powder XRD patterns and refinement of PrSbTe. Powder sample was obtained by grounding the single crystals. (d) Magnetic susceptibility and inverse magnetic susceptibility of PrSbTe with $H//c$ as a function of temperature, measured with the magnetic field of 0.1 T. The red dashed line represents the Curie-Weiss fits for $T > 100$ K. μ_{eff} is effective moment, and Θ is the Weiss temperature. (e) Field dependence of magnetization as a function of applied magnetic fields of PrSbTe at $T = 0.4$ K with $H//c$. (f) Temperature dependence of the specific heat C_p of PrSbTe. The inset is linear fit for C_p/T vs T^2 at low temperatures. γ is the Sommerfeld coefficient, and Θ_D is the Debye temperature.

*Ln*SbTe compounds [26]. A comprehensive investigation of the electronic structure of PrSbTe is imperative to understand the above difference.

The three-dimensional Brillouin zone of PrSbTe has three independent high-symmetry lines: Γ-X, Γ-M, and Γ-Z, as illustrated in Fig. 2(a). The high-symmetry points are marked on both the bulk and surface Brillouin zones. By varying photon energies ranging from $h\nu$= 65 to 130 eV in the ARPES measurements, the $k_x - k_z$ Fermi surface (FS) maps and constant energy contours with an energy window of 10 meV were obtained, as shown in Fig. 2(b). According to the periodicity of the band structure in the k_z direction, we can determine that the momentum cuts taken with $h\nu$= 95 and 83 eV cross $k_z = 0$ and π, respectively. The $k_x - k_z$ FS exhibits multiple parallel lines, revealing strong two-dimensional characteristics of the electronic structure of PrSbTe along the k_z direction. Because of the weak interlayer coupling, ARPES spectra of PrSbTe show weak k_z dispersion, which is like the two-dimensional characteristics of FS reported in isomorphic compounds, such as ZrSiS [40] and CeSbTe [41].

Figures 2(c) and 2(d) show the $k_x - k_y$ FS mapping and constant energy contours taken with the photon energies of 95 and 83 eV, respectively. Whether for $k_z = 0$ or $k_z = \pi$, we can clearly see a large diamond-shaped FS centered around the Γ or Z point, which appears like the other *Ln*SbTe compounds [17–19]. The spectral weight at the apex of the diamond-shaped FS is significantly pronounced, suggesting that PrSbTe may support small electronic pockets at the X and R points. The diamond-shaped pocket consists of two sheets: the inner sheet exhibiting a strong spectral weight, but the outer one appears relatively indistinct. With increasing binding energy, the sheet separation in the momentum space reduces and finally turns into a single sheet at 450 meV below the Fermi level. Apart from the diamond-shaped features, the evolution of constant energy contours with binding energy has obvious differences for the two photon energies $h\nu$= 95 and 83 eV. In the Γ-X-M plane with $h\nu$= 95 eV, a circular feature appears around the Γ point at 300 meV below the Fermi level. As the binding energy increases, the circular feature expands in size and evolves into a diamond-shaped topology at 450, 600, and 900 meV below the Fermi level. In contrast, the circular feature in the Z-R-A plane with $h\nu$= 83 eV is vague but eventually evolves into a new diamond-shaped structure as well. Altogether, the FS of PrSbTe is like previously reported data on other *Ln*SbTe materials [17–22].

The calculated bulk band structure is shown in Fig. 3(a), and SOC is considered. There are three primary bands near the Fermi level, labeled α, β, and η. The formation of Dirac nodes in PrSbTe can be directly observed from the calculated band structures. In the Γ-X direction, two Dirac nodes can be

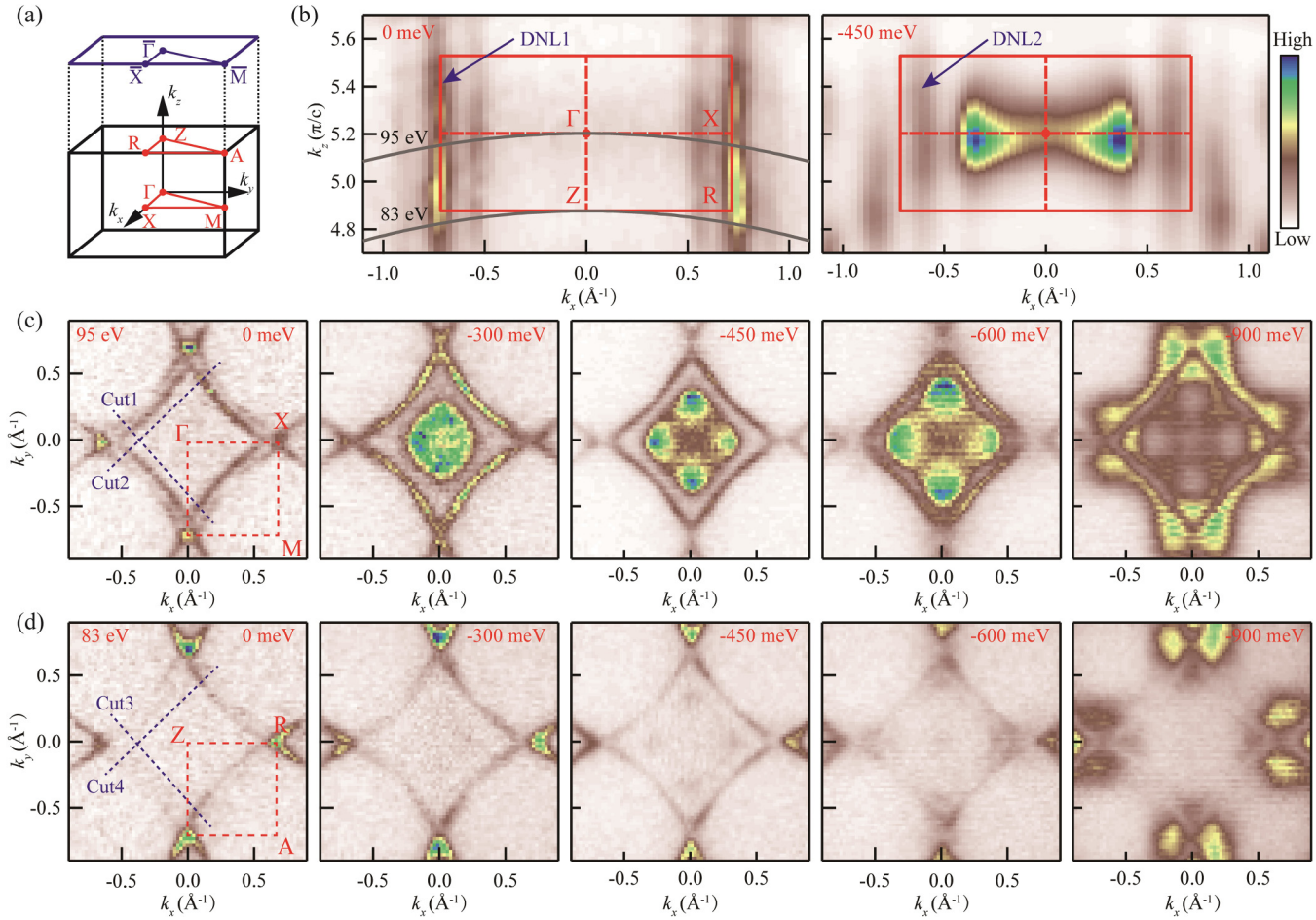

FIG. 2. (a) Bulk Brillouin zone and the projected surface Brillouin zone of PrSbTe. High-symmetry points are marked. (b) The $k_x - k_z$ Fermi surface (FS; left) and constant energy contour (right) at $E - E_F = -450$ meV of PrSbTe obtained by the photon energy scanning under linear horizontal (LH) polarization. With the inner potential $V_0 = 13$ eV, the relative position of the first Brillouin zone is indicated by the red box. The momentum cuts taken with 95 and 83 eV have been marked with gray lines, which cross the Γ and Z points, respectively (left). (c) The $k_x - k_y$ FSs and constant energy contours of PrSbTe with various binding energies measured at the photon energy of 95 eV under LH polarization. (d) The $k_x - k_y$ FSs and constant energy contours of PrSbTe with various binding energies measured at the photon energy of 83 eV under LH polarization.

observed: one is near the X point from the $\alpha - \beta$ band, and the other one locates at 450 meV below the Fermi level, which is from the $\beta - \eta$ band. Noteworthy, a third Dirac node can be found in the Γ-M direction, which is also near the Fermi level and formed by the $\beta - \eta$ band. These Dirac nodes derived from the $\alpha - \beta$ band manifest gapless crossings at the X and R points, but the ones derived from the $\beta - \eta$ band have gaps of > 10 meV. Moreover, the upper branches of the Dirac nodes originating from the $\beta - \eta$ band contribute to the formation of a two-sheet feature of the diamond-shaped FS, as illustrated in Fig. 2(c). We also show the calculated density of states in Fig. 3(a). At the Fermi level, the calculation yields $N(E_F) = 0.6335$ states/(eV f.u.), or equivalently $\gamma_0 = 1.49\,\mathrm{mJ/mol\,K^2}$. These states are dominated by the Sb$-5p$ and Te$-5p$ orbitals, with certain contribution from Pr$-5d$ orbitals.

A photoemission intensity cut along the X-Γ-X direction at $k_z = 0$ is shown in Fig. 3(b). We can see that multiple linearly dispersive bands are near the X point, and the Dirac nodes align well with the calculated results. Especially the Dirac node formed from the $\alpha - \beta$ band lies exactly at the X point, and its energy position is rather close to the Fermi level. Moreover, the η band forms a holelike pocket around the Γ point, corresponding to the circular feature at the constant energy contours, as observed in Fig. 2(c). The dispersion map along the R-Z-R direction at $k_z = \pi$ are presented in Fig. 3(c). The bands along this direction exhibit significant difference with varying photon energies, indicating their bulk nature. Fortunately, the primary α, β, and η bands maintain similar characteristics to the X-Γ-X direction. Figure 3(e) displays representative band structures around the $\bar{X}$ point measured at photon energies ranging from 83 to 95 eV, corresponding to a half$-k_z$ period. The Dirac-like structure can be observed in all the measurements using different photon energies, as marked by the dashed lines in Fig. 3(e). Combined with the schematic of DNLs shown in Fig. 3(d), we can determine two DNLs along the X-R direction, which are marked as DNL1 and DNL2 in Fig. 2(b). It is worth noting that the binding energy of the Dirac nodes changes slightly with the photon energies, and the Dirac node formed from the $\alpha - \beta$

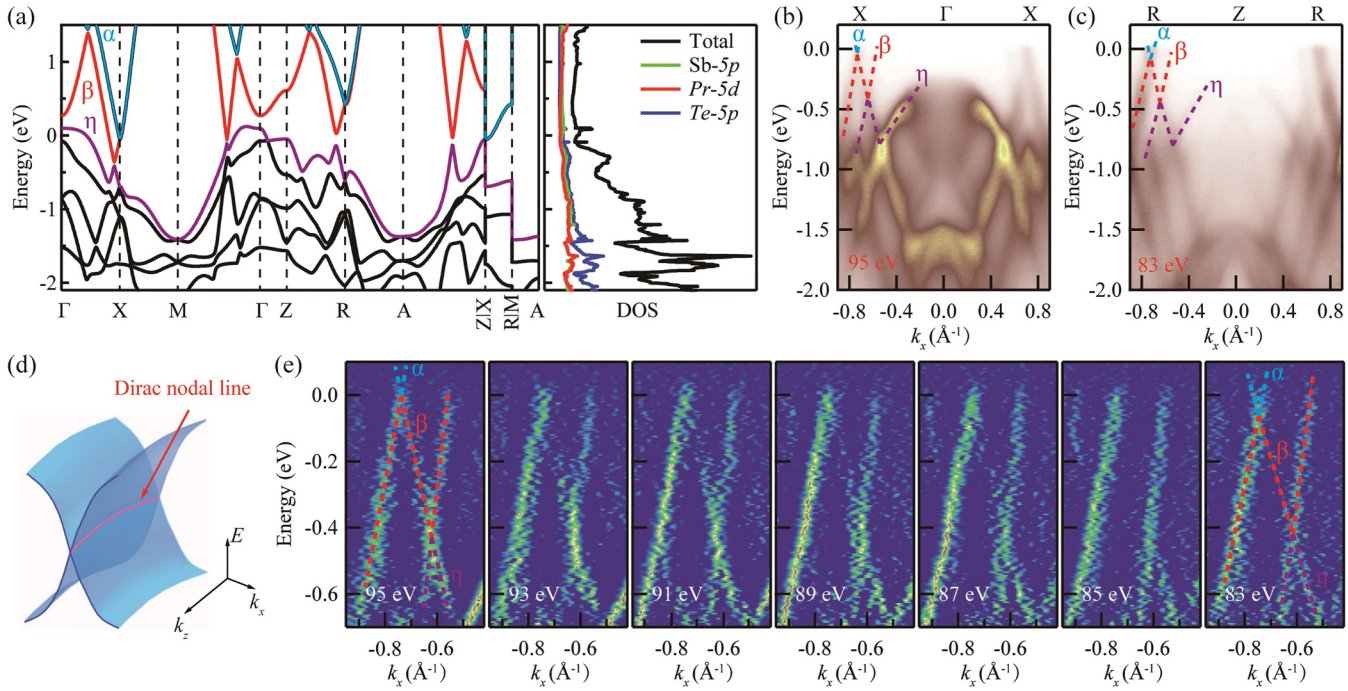

FIG. 3. (a) Calculated bulk bands (left) and density of states (right), and spin-orbit coupling (SOC) is considered. The blue, red, and purple lines highlight the primary bands close to the Fermi level, labeled α, β, and η, respectively. (b) Photoemission intensity cut along X-Γ-X measured at the photon energy $h\nu$= 95 eV. The three primary bands in (a) are marked with dotted lines, in correspondence with theoretical calculations in (a). (c) Photoemission intensity cut along R-Z-R measured at the photon energy of 83 eV. (d) Schematic of the band structure hosting a Dirac nodal line along the k_z direction. (e) Partial enlarged second derivative maps around the $\bar{X}$ point with different photon energies. The photon energies are noted in the plots, and the dotted lines mark the branches of the linearly dispersed Dirac bands.

band at the R point is $\sim$ 80 meV lower than that at the X point. From the bulk calculations presented in Fig. 3(a), the energy difference of the Dirac points at X and R is $\sim$ 0.5 eV. According to the universal curve that describes the general behavior of the inelastic mean free path of electrons in solids [42], the probing depth for the photons between 80 and 100 eV is $\sim$ 7 Å, which causes a pronounced k_z broadening effect, so similar band structures could be observed in different k_z planes.

For the band structure along the M-Γ-M direction at $k_z = 0$, a linearly dispersive band with large Fermi velocity seems to cross the Fermi level, as shown in Fig. 4(a), which gives rise to the outer sheet of the diamond-shaped Fermi pocket. The experimental band structures agree with our calculated results [Fig. 3(a)]. According to the calculated bulk band structure [Fig. 3(a)], the linearly dispersive band is originated from the Dirac node formed by the $\beta-\eta$ band. Similar band dispersion is observed in the ARPES map along the A-R-A direction at $k_z = \pi$, which is measured at a photon energy of 83 eV, as shown in Fig. 4(d). To observe the detail of the linearly dispersive bands near the Fermi level, zoomed-in dispersion cuts along and parallel to the M-Γ-M and A-Z-A directions are shown in Figs. 4(c) and 4(d), respectively. Notably, only one branch along the M-Γ-M direction can be observed with the photon energy of 95 eV, whereas two branches of the Dirac state can be observed with the photon energy of 83 eV. The difference in the band intensity with the photon energy originates from the photoemission matrix element effects. Meanwhile, two branches of the Dirac state can be clearly seen in the dispersion cuts parallel to the M-Γ-M direction, and they form the two-sheet feature of the diamond-shaped FS in Fig. 2(c). The dispersion maps along the M-X-M and A-R-A direction, which show the Dirac-like states with their nodes locating at $\sim$ 770 meV below the Fermi level, are presented in Figs. 4(e) and 4(f), respectively. Since there are no Dirac crossings observed along the X-M and R-A directions in the bulk calculations depicted in Fig. 3(a) and considering the previous observation of similar surface states in ZrSiS [40] and the LnSbTe families [21,22], it can be inferred that these states originate from the surface.

Finally, we performed on- and off-resonant ARPES spectra along the $\bar{X} - \bar{\Gamma} - \bar{X}$ direction to probe the $4f$-specific spectral function, as shown in Figs. 5(a) and 5(b), respectively. The off-resonant ARPES spectrum ($h\nu$= 95 eV) predominantly exhibits emission from the conduction bands, and the resonant spectrum ($h\nu$= 124 eV) significantly amplifies the $4f$ spectral weight. The on-resonant spectrum features two broad $4f$ bands, one at 4.7 eV and the other at 1.6 eV below the Fermi level, as presented in Fig. 5(c). The flat band at 4.7 eV binding energy with strong intensity can be assigned to the initial $4f^0$ state, whose energy is deeper than the sister compound CeSbTe [41]. Based on the single-impurity Anderson model, a deeper $4f^0$ peak indicates the more localized nature of $4f$ electrons [43]. As mentioned above, the specific heat measurement reveals a Sommerfeld coefficient γ of 2.6231 mJ/mol K^2, which is significantly smaller than other sister compounds with $4f$ electrons. We note the calculated γ_0 = 1.49 mJ/mol K^2, which corresponds to a small mass renormalization factor $m^*/m \sim 1.76$ even without considering the electron-phonon coupling contribution. These

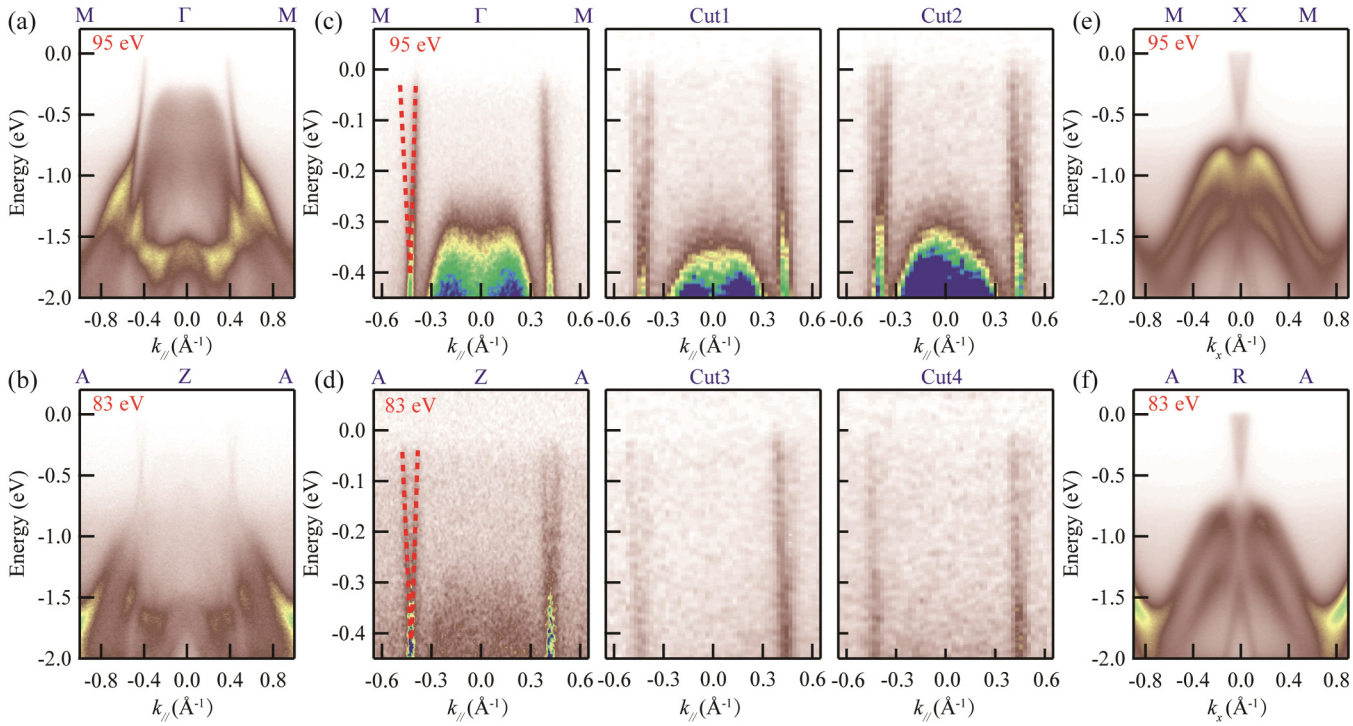

FIG. 4. (a) Photoemission intensity cut along the *M*-Γ-*M* direction measured at the photon energy of 95 eV. (b) Photoemission intensity cut along the *A*-*Z*-*A* direction measured at the photon energy of 83 eV. (c) Zoomed-in band structure along the *M*-Γ-*M* direction and two parallel directions [Cut1, Cut2 marked in Fig. 2(c)]. (d) Zoomed-in band structure along *A*-*Z*-*A* direction and two parallel directions [Cut3, Cut4 marked in Fig. 2(d)]. (e) Photoemission intensity cut along the *M*-*X*-*M* direction measured at the photon energy of 95 eV. (f) Photoemission intensity cut along the *A*-*R*-*A* direction measured at the photon energy of 83 eV.

observations provide additional evidence supporting the localized state of the 4*f* electrons. Furthermore, our experimental results agree with the calculated band structure considering the Pr 4*f* electrons as localized core electrons, thereby providing additional validation for this assertion. In addition, the momentum-integrated energy distribution curve (EDC) measured with on-resonant photon energy is shown in Fig. 5(d), which reveals expected core levels including Te 4*d*, Sb 4*d*, and Pr 5*p* and 4*f* peaks. This is in analogous to other members of the *Ln*SbTe family of materials, such as CeSbTe [41] and GdSbTe [17].

IV. DISCUSSION

In this paper, the topological nodal line states in PrSbTe are directly observed by ARPES measurements, which show some similarities with the ZrSiS family and other *Ln*SbTe compounds. For example, they all exhibit a large diamond-shaped FS and pronounced two-dimensional electronic character. However, differences in details can also be found in PrSbTe, compared with other *Ln*SbTe systems. For example, two-sheet FS topology in PrSbTe is clearly observed, while in GdSbTe [17] and HoSbTe [18], only

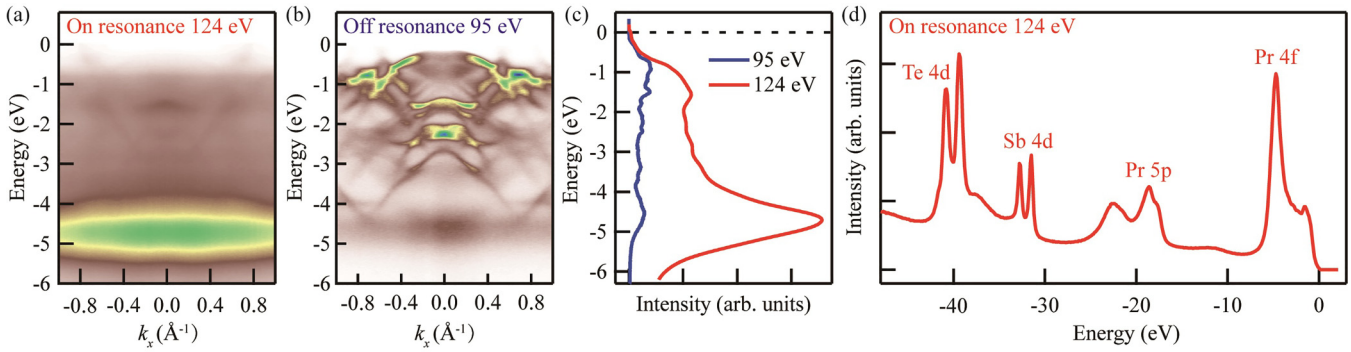

FIG. 5. (a) On-resonant angle-resolved photoemission spectroscopy (ARPES) spectra along the *X*-Γ-*X* direction measured at photon energy $h\nu$= 124 eV. (b) Off-resonant ARPES spectra along the *X*-Γ-*X* direction measured at photon energy $h\nu$= 95 eV. (c) Integrated energy distribution curves (EDCs) of on- and off-resonant ARPES spectra. (d) Momentum integrated EDC of PrSbTe taken with on-resonant photon energy.

single-sheet diamond-shaped FS is revealed. In both ZrSiS and *Ln*SbTe compounds, the Dirac points arise from the bulk band crossings and form the DNLs in momentum space, as observed by both band calculations and ARPES measurements. However, in comparison with the ZrSiS and HfSiS compounds [44], where the DNLs are located ~ 0.6 eV below the Fermi level, the nodal lines in *Ln*SbTe compounds locate right near the Fermi level, and furthermore, they exhibit a robust character at the Brillouin zone boundary. In PrSbTe, a gapless DNL along the *X*-*R* direction is clearly found near the Fermi level by our ARPES experiments. Although bulk band calculations reveal that the consideration of SOC induces energy gaps in certain Dirac nodes and DNLs of the *Ln*SbTe system, these energy gaps are not directly observed due to limitation in the energy resolution of ARPES measurements.

CDW has been confirmed to exist in $CeSb_xTe_{2-x-\delta}$ [28], $NdSb_xTe_{2-x-\delta}$ [29], and $GdSb_xTe_{2-x-\delta}$ [30,32] and is related to the components of Sb by XRD, transmission electron microscopy (TEM), and neutron diffraction measurements. Also, ARPES measurements revealed the two-sheet characteristics of the FS and an opening of the gap along the Γ-*M* direction in CeSbTe, suggesting a connection to the FS nesting induced by CDW order [41], while in ZrSiS [40] and HfSiS [45], they are considered to be derived from the surface states, which has been confirmed by the bulk-sensitive soft x-ray ARPES measurements. In this paper, although the two FS sheets are also observed in PrSbTe, bulk band calculations clearly indicate that they originate from the α, β, and η bands near the Fermi level with no gap opening. Whether the CDW orders exist in the stoichiometric *Ln*SbTe compounds remains an open question, which needs a combined study with other experimental methods, such as low-energy electron diffraction, scanning tunneling microscopy, TEM, and neutron diffraction measurements.

Although the band structures and FS characteristics of PrSbTe by off-resonanat ARPES closely resemble those of other *Ln*SbTe compounds, on-resonant ARPES data in PrSbTe observe a flat band at 4.7 eV below the Fermi level that is assigned to the initial Pr $4f^0$ state, indicating the localized nature of the $4f$ electrons. Also, the Sommerfeld coefficient γ derived from the specific heat measurements is $2.6231\,\mathrm{mJ/mol\,K^2}$, consistent with the DFT-calculated $\gamma_0 = 1.49\,\mathrm{mJ/mol\,K^2}$, which is comparable with LaSbTe without $4f$ electrons but much lower than other *Ln*SbTe compounds with $4f$ electrons. This suggests that the localized state of $4f$ electrons in the *Ln*SbTe system does not significantly impact the band topology.

Specific heat and magnetic measurements reveal that PrSbTe exhibits no phase transition and remains in a paramagnetic ground state even down to 0.4 K. However, other *Ln*SbTe compounds with $4f$ electrons all exhibit rich magnetic orders. For example, CeSbTe [16] and GdSbTe [23] exhibit AFM < 2.7 and 12 K, respectively, even accompanied by metamagnetic transitions. For *Ln*SbTe compounds, which are protected by nonsymmorphic symmetry, the introduction of magnetism breaks the time-reversal symmetry, thereby tuning the electronic structure and driving them through a manifold of topologically distinct phases [16]. The absence of magnetism in PrSbTe down to 0.4 K may be attributed to the difference in crystal structure parameters, the strength of SOC, and the outer electron configuration of the Pr atom. Therefore, the *Ln*SbTe system can serve as a comprehensive platform for investigating the competition among magnetic order, SOC, CDW, electron correlation, and topological states. Moreover, the substitution of *Ln* elements plays a crucial role in adjusting this competitive relationship.

V. CONCLUSIONS

In summary, we carried out a combined study with ARPES, magnetic measurements, specific heat, and band structure calculations to investigate the electronic structures of PrSbTe. The $4f$ electrons of Pr are treated as localized core electrons, and SOC is considered in the band structure calculations, which is in excellent agreement with experimental results obtained from ARPES measurements. Typical ZrSiS-type diamond-shaped FS and multiple DNLs are observed, which is like other *Ln*SbTe compounds. The small Sommerfeld coefficient derived from specific heat measurements and the high banding energy of the $4f^0$ band in the on-resonant ARPES spectrum indicate the localized nature of $4f$ in PrSbTe. In this paper, we provide an additional platform for comprehending the electronic structure within the *Ln*SbTe subfamily of materials, thereby facilitating the exploration of phenomena and potential applications associated with nodal line semimetals.

ACKNOWLEDGMENTS

This paper was supported by the National Key Research and Development Program of China (Grants No. 2022YFA1402201 and No. 2021YFA1601101), the National Science Foundation of China (Grants No. 12122409, No. 11974319, and No. 11904335), the Fund of Science and Technology on Surface Physics and Chemistry Laboratory (No. XKFZ202106), and the Special Talent Fund of the Institute of Materials (No. TP03201901). ARPES measurements were performed in the ARPES endstation of BL03U and BL09U of SSRF, China. The magnetic and specific heat measurements were performed in the Synergetic Extreme Condition User Facility.

[1] W. Tremel and R. Hoffmann, Square nets of main-group elements in solid-state materials, J. Am. Chem. Soc. **109**, 124 (1987).

[2] S.-Y. Yang, H. Yang, E. Derunova, S. S. P. Parkin, B. Yan, and M. N. Ali, Symmetry demanded topological nodal-line materials, Adv. Phys. X. **3**, 1414631 (2018).

[3] S. M. Young and C. L. Kane, Dirac semimetals in two dimensions, Phys. Rev. Lett. **115**, 126803 (2015).

[4] S. Klemenz, S. Lei, and L. M. Schoop, Topological semimetals in square-net materials, Ann. Rev. Mater. Res. **49**, 185 (2019).

[5] C. C. Tsuei and J. R. Kirtley, Pairing symmetry in cuprate superconductors, Rev. Mod. Phys. **72**, 969 (2000).

[6] J. Paglione and R. L. Greene, High-temperature superconductivity in iron-based materials, Nat. Phys. **6**, 645 (2010).

[7] G. R. Stewart, Superconductivity in iron compounds, Rev. Mod. Phys. **83**, 1589 (2011).

[8] D. N. Basov and A. V. Chubukov, Manifesto for a higher T_c, Nat. Phys. **7**, 272 (2011).

[9] J. Hu, Z. Tang, J. Liu, X. Liu, Y. Zhu, D. Graf, K. Myhro, S. Tran, C. N. Lau, J. Wei *et al.*, Evidence of topological nodal-line fermions in ZrSiSe and ZrSiTe, Phys. Rev. Lett. **117**, 016602 (2016).

[10] S. Pezzini, M. R. van Delft, L. M. Schoop, B. V. Lotsch, A. Carrington, M. I. Katsnelson, N. E. Hussey, and S. Wiedmann, Unconventional mass enhancement around the Dirac nodal loop in ZrSiS, Nat. Phys. **14**, 178 (2018).

[11] J. Ebad-Allah, J. F. Afonso, M. Krottenmüller, J. Hu, Y. L. Zhu, Z. Q. Mao, J. Kuneš, and C. A. Kuntscher, Chemical pressure effect on the optical conductivity of the nodal-line semimetals ZrSiY (Y = S, Se, Te) and ZrGeY (Y = S, Te), Phys. Rev. B **99**, 125154 (2019).

[12] X. Wang, X. Pan, M. Gao, J. Yu, J. Jiang, J. Zhang, H. Zuo, M. Zhang, Z. Wei, W. Niu *et al.*, Evidence of both surface and bulk Dirac bands and anisotropic nonsaturating magnetoresistance in ZrSiS, Adv. Electron. Mater. **2**, 1600228 (2016).

[13] R. Singha, A. K. Pariari, B. Satpati, and P. Mandal, Large nonsaturating magnetoresistance and signature of nondegenerate Dirac nodes in ZrSiS, Proc. Natl. Acad. Sci. USA **114**, 2468 (2017).

[14] R. Sankar, G. Peramaiyan, I. P. Muthuselvam, C. J. Butler, K. Dimitri, M. Neupane, G. N. Rao, M. T. Lin, and F. C. Chou, Crystal growth of Dirac semimetal ZrSiS with high magnetoresistance and mobility, Sci. Rep. **7**, 40603 (2017).

[15] M. Matusiak, J. R. Cooper, and D. Kaczorowski, Thermoelectric quantum oscillations in ZrSiS, Nat. Commun. **8**, 15219 (2017).

[16] L. M. Schoop, A. Topp, J. Lippmann, F. Orlandi, L. Muchler, M. G. Vergniory, Y. Sun, A. W. Rost, V. Duppel, M. Krivenkov *et al.*, Tunable Weyl and Dirac states in the nonsymmorphic compound CeSbTe, Sci. Adv. **4**, eaar2317 (2018).

[17] M. M. Hosen, G. Dhakal, K. Dimitri, P. Maldonado, A. Aperis, F. Kabir, C. Sims, P. Riseborough, P. M. Oppeneer, D. Kaczorowski *et al.*, Discovery of topological nodal-line fermionic phase in a magnetic material GdSbTe, Sci. Rep. **8**, 13283 (2018).

[18] S. Yue, Y. Qian, M. Yang, D. Geng, C. Yi, S. Kumar, K. Shimada, P. Cheng, L. Chen, Z. Wang *et al.*, Topological electronic structure in the antiferromagnet HoSbTe, Phys. Rev. B **102**, 155109 (2020).

[19] Y. Wang, Y. T. Qian, M. Yang, H. X. Chen, C. Li, Z. Y. Tan, Y. Q. Cai, W. J. Zhao, S. Y. Gao, Y. Feng *et al.*, Spectroscopic evidence for the realization of a genuine topological nodal-line semimetal in LaSbTe, Phys. Rev. B **103**, 125131 (2021).

[20] K. Pandey, D. Mondal, J. W. Villanova, J. Roll, R. Basnet, A. Wegner, G. Acharya, M. R. U. Nabi, B. Ghosh, J. Fujii *et al.*, Magnetic topological semimetal phase with electronic correlation enhancement in SmSbTe, Adv. Quantum Technol. **4**, 2100063 (2021).

[21] S. Regmi, G. Dhakal, F. C. Kabeer, N. Harrison, F. Kabir, A. P. Sakhya, K. Gofryk, D. Kaczorowski, P. M. Oppeneer, M. Neupane *et al.*, Observation of multiple nodal lines in SmSbTe, Phys. Rev. Mater. **6**, L031201 (2022).

[22] S. Regmi, R. Smith, A. P. Sakhya, M. Sprague, M. I. Mondal, I. B. Elius, N. Valadez, A. Ptok, D. Kaczorowski, and M. Neupane, Observation of gapless nodal-line states in NdSbTe, Phys. Rev. Mater. **7**, 044202 (2023).

[23] R. Sankar, I. P. Muthuselvam, K. R. Babu, G. S. Murugan, K. Rajagopal, R. Kumar, T. Wu, C. Wen, W. Lee, G. Guo *et al.*, Crystal growth and magnetic properties of topological nodal-line semimetal GdSbTe with antiferromagnetic spin ordering, Inorg. Chem. **58**, 11730 (2019).

[24] K. Pandey, R. Basnet, A. Wegner, G. Acharya, M. R. U. Nabi, J. Liu, J. Wang, Y. K. Takahashi, B. Da, J. Hu *et al.*, Electronic and magnetic properties of the topological semimetal candidate NdSbTe, Phys. Rev. B **101**, 235161 (2020).

[25] M. Yang, Y. Qian, D. Yan, Y. Li, Y. Song, Z. Wang, C. Yi, H. L. Feng, H. Weng, and Y. Shi, Magnetic and electronic properties of a topological nodal line semimetal candidate: HoSbTe, Phys. Rev. Mater. **4**, 094203 (2020).

[26] F. Gao, J. Huang, W. Ren, M. Li, H. Wang, T. Yang, B. Li, and Z. Zhang, Magnetic and transport properties of the topological compound DySbTe, Phys. Rev. B **105**, 214434 (2022).

[27] F. Gao, J. Huang, W. Ren, H. Wu, M. An, X. Wu, L. Zhang, T. Yang, A. Wang, Y. Chai *et al.*, Magnetic and magnetotransport properties of the magnetic topological nodal-line semimetal TbSbTe, Adv. Quantum Technol. **6**, 2200163 (2023).

[28] R. Singha, T. H. Salters, S. Teicher, S. M. Lei, J. F. Khoury, N. P. Ong, and L. M. Schoop, Evolving devil's staircase magnetization from tunable charge density waves in nonsymmorphic Dirac semimetals, Adv. Mater. **33**, 2103476 (2021).

[29] T. H. Salters, F. Orlandi, T. Berry, J. F. Khoury, E. Whittaker, P. Manuel, and L. M. Schoop, Charge density wave-templated spin cycloid in topological semimetal $NdSb_xTe_{2-x-\delta}$, Phys. Rev. Mater. **7**, 044203 (2023).

[30] R. J. Kirby, A. Montanaro, F. Giusti, A. Koch-Liston, S. Lei, I. Petrides, P. Narang, K. S. Burch, D. Fausti, G. D. Scholes *et al.*, Ultrafast dynamics of the topological semimetal $GdSb_xTe_{2-x-\delta}$ in the presence and absence of a charge density wave, J. Phys. Chem. C **127**, 577 (2023).

[31] E. DiMasi, B. Foran, M. C. Aronson, and S. Lee, Stability of charge-density waves under continuous variation of band filling in $LaTe_{2-x}Sb_x$ ($0 \leqslant x \leqslant 1$), Phys. Rev. B **54**, 13587 (1996).

[32] S. Lei, V. Duppel, J. M. Lippmann, J. Nuss, B. V. Lotsch, and L. M. Schoop, Charge density waves and magnetism in topological semimetal candidates $GdSb_xTe_{2-x-\delta}$, Adv. Quantum Technol. **2**, 1900045 (2019).

[33] Y. Yang, Z. Liu, J. Liu, Z. Liu, W. Liu, X. Lu, H. Mei, A. Li, M. Ye, S. Qiao *et al.*, High-resolution ARPES endstation for *in situ* electronic structure investigations at SSRF, Nucl. Sci. Tech. **32**, 31 (2021).

[34] G. Kresse and J. Furthmüller, Efficiency of *ab-initio* total energy calculations for metals and semiconductors using a plane-wave basis set, Comput. Mater. Sci. **6**, 15 (1996).

[35] G. Kresse and J. Furthmüller, Efficient iterative schemes for *ab initio* total-energy calculations using a plane-wave basis set, Phys. Rev. B **54**, 11169 (1996).

[36] J. P. Perdew, K. Burke, and M. Ernzerhof, Generalized gradient approximation made simple, Phys. Rev. Lett. **77**, 3865 (1996).

[37] X. C. Wang, Q. Q. Liu, Y. X. Lv, W. B. Gao, L. X. Yang, R. C. Yu, F. Y. Li, and C. Q. Jin, The superconductivity at 18 K in LiFeAs system, Solid State Commun. **148**, 538 (2008).

[38] J. Charvillat, D. Damien, and A. Wojakowski, Crystal chemistry of binary MSb_2 and ternary MSbTe compounds of transuranium elements, Revue. De. Chimie. Minerale. **14**, 178 (1977).

[39] B. J. Lv, J. Chen, L. Qiao, J. Ma, X. H. Yang, M. C. Li, M. M. Wang, Q. Tao, and Z. A. Xu, Magnetic and transport properties of low-carrier-density Kondo semimetal CeSbTe, J. Phys.: Condes. Matter **31**, 355601 (2019).

[40] B. B. Fu, C. J. Yi, T. T. Zhang, M. Caputo, J. Z. Ma, X. Gao, B. Q. Lv, L. Y. Kong, Y. B. Huang, P. Richard *et al.*, Dirac nodal surfaces and nodal lines in ZrSiS, Sci. Adv. **5**, 6459 (2019).

[41] P. Li, B. Lv, Y. Fang, W. Guo, Z. Wu, Y. Wu, D. Shen, Y. Nie, L. Petaccia, C. Cao *et al.*, Charge density wave and weak Kondo effect in a Dirac semimetal CeSbTe, Sci. China Phys. Mech. Astron. **64**, 237412 (2021).

[42] S. Fujimori, Y. Takeda, T. Okane, Y. Saitoh, A. Fujimori, H. Yamagami, Y. Haga, E. Yamamoto, and Y. Ōnuki, Electronic structures of uranium compounds studied by soft x-ray photoelectron spectroscopy, J. Phys. Soc. Jpn. **85**, 062001 (2016).

[43] S. Kirchner, S. Paschen, Q. Chen, S. Wirth, D. Feng, J. D. Thompson, and Q. Si, Colloquium: Heavy-electron quantum criticality and single-particle spectroscopy, Rev. Mod. Phys. **92**, 011002 (2020).

[44] C. Chen, X. Xu, J. Jiang, S.-C. Wu, Y. P. Qi, L. X. Yang, M. X. Wang, Y. Sun, N. B. M. Schröter, H. F. Yang *et al.*, Dirac line nodes and effect of spin-orbit coupling in the nonsymmorphic critical semimetals MSiS (M = Hf, Zr), Phys. Rev. B **95**, 125126 (2017).

[45] D. Takane, Z. Wang, S. Souma, K. Nakayama, C. X. Trang, T. Sato, T. Takahashi, and Y. Ando, Dirac-node arc in the topological line-node semimetal HfSiS, Phys. Rev. B **94**, 121108(R) (2016).